6th European Conference on Computational Mechanics (ECCM 6)
7th European Conference on Computational Fluid Dynamics (ECFD 7)
1115 June 2018, Glasgow, UK

HIGH-ORDER DG SOLUTIONS OF SEPARATING AND REATTACHING FLOWS

A. CIMARELLI, M. FRANCIOLINI and A. CRIVELLINI

DIISM, Università Politecnica delle Marche
Via Brecce Bianche, 60131, Ancona, Italy
{a.cimarelli@staff, m.franciolini@staff, a.crivellini@staff}.univpm.it

Key words: Separating and reattaching flows, Large scale unsteadinesses, Discontinuous Galerkin, ILES

Abstract. We report high-order implicit Large Eddy Simulations of flows around elongated bluff bodies with massive flow separation and reattachment. The aim is to provide evidence of the influence of relevant flow parameters such as the geometry of the leading-edge corners and the presence or not of a trailing-edge flow separation, on the behaviour of the initially laminar recirculating flow. Attention will be devoted also on the possible repercussions of such a results on the understanding of the nature of the main unsteadinesses of separating and reattaching flows. We finally prove the computational efficiency and the reliability of the proposed solution strategy for the time implicit high-order Discontinuous Galerkin (DG) discretization of the three-dimensional incompressible Navier-Stokes equations. The algorithm uses a linearly implicit Runge-Kutta scheme of the Rosenbrock type, and a p-multigrid preconditioned matrix-free linear solver.

1 INTRODUCTION

One of the main feature of separating and reattaching flows is the combined presence of small scales due to the occurrence of turbulence and large scales due to phenomena of shedding of large-scale vortices. These phenomena nonlinearly interact themselves giving rise to a self-sustained cycle. Two main large-scale unsteadinesses are recognized: the shedding of vortices from the leading-edge shear layer and the low-frequency flapping mode of the recirculating region [1]. Despite the fact that these kind of phenomena have been the subject of several numerical and experimental studies, their nature is still elusive and deserves further investigations. Indeed, a deeper understanding of the origin of the main unsteadinesses of separating and reattaching flow may have strong repercussions on the development of control strategies relevant for a huge number of applications in natural and engineering sciences. Here, we aim at providing a further develop on the knowledge of such phenomena.

Numerical experiments have radically changed the approach to fluid dynamics. As an example, numerical simulations generally allow for broad observational capabilities that experiments cannot give. Another important feature of numerical experiments is

the ability to manipulate the flow in order to remove/suppress or add/enhance physical processes and to measure the effects of those modifications on the dynamics of the flow. In this work, we make use of this ability in order to identify the main parameters controlling separating and reattaching flows and to understand the physical origin of the related mechanisms. In particular, we start by considering the flow around a rectangular cylinder (*run1*) which is recognized to be a very simple flow configuration for the analysis of separated and reattaching flow [2, 3, 4, 5, 6, 7]. In order to appreciate the effects of shedding phenomena at the trailing edge on the behaviour of the main recirculating region, we then consider the flow around an infinite plate with right-angled (*run2*). As shown in [8, 9, 10], also this flow is recognized to be of overwhelming interest for the study of large scale recirculating flows. Regarding the case of infinite plates with leading edge separation bubble we also address the effect of the leading-edge geometry on the physics of the recirculating region, by considering also an infinite flat plate with circular leading-edge corner (*run3*). Overall, the simulation of the above mentioned three type of separating and reattaching flows would allows us to identify the role played by the geometry of the leading-edge corner and of the presence or not of a trailing-edge flow separation, on the dynamics of the recirculating flow. A sketch of the flow configurations is reported in figure 1.

Finally, by considering a fourth type of simulation, we also aim at understanding the nature of the so-called large-scale unsteadiness [1]. It consists of a very slow flapping mode of the recirculating bubble. The unsteadiness at the basis of this enlargement and shrinkage of the recirculating region, could take origin from coupling phenomena between the shedding of large-scale vortices from the recirculating flows in the two sides of the plate. To understand this, the fourth type of simulation (*run4*) reproduces the separating and reattaching flow over an infinite plate with circular leading edge such as (*run3*) but removing possible interactions between the two sides of the plate by applying a symmetry boundary condition in the half horizontal plane of the domain, see again figure 1.

2 THE NUMERICAL PROCEDURE

For the numerical experiments, the set of the incompressible Navier–Stokes (INS) equations is solved using an implicit LES approach. In other words, the approach relies on the dissipation properties of the numerical scheme without the use of an explicit SGS model. The numerical method is based on a modal DG framework with orthonormal, hierarchical basis functions, thus the mass matrix is the identity, defined in the physical space. The solver relies on a triangulation $\mathcal{T}_h$ of the domain Ω. The state vector is assumed to be a polynomial expansion with no continuity constraints imposed on the approximations on adjacent elements $\mathbf{u}_h \in [\mathcal{V}_h]^M$ where $\mathcal{V}_h = \{u \in L_2(\Omega) : u|_K \in \mathbb{P}_k, \forall K \in \mathcal{T}_h\}$, $M = 4$ is the number of equations of the model and k is the order of polynomial approximation. The weak-form of the incompressible Navier–Stokes equations follows from multiplying the set of PDEs by test functions in the same approximation space, integrating by parts, and coupling elements via consistent and stable numerical fluxes. The artificial viscosity flux approach [15, 14, 17] and the second form of the Bassi–Rebay scheme (BR2) [16] are employed for the convective and diffusive terms, respectively. By following this procedure

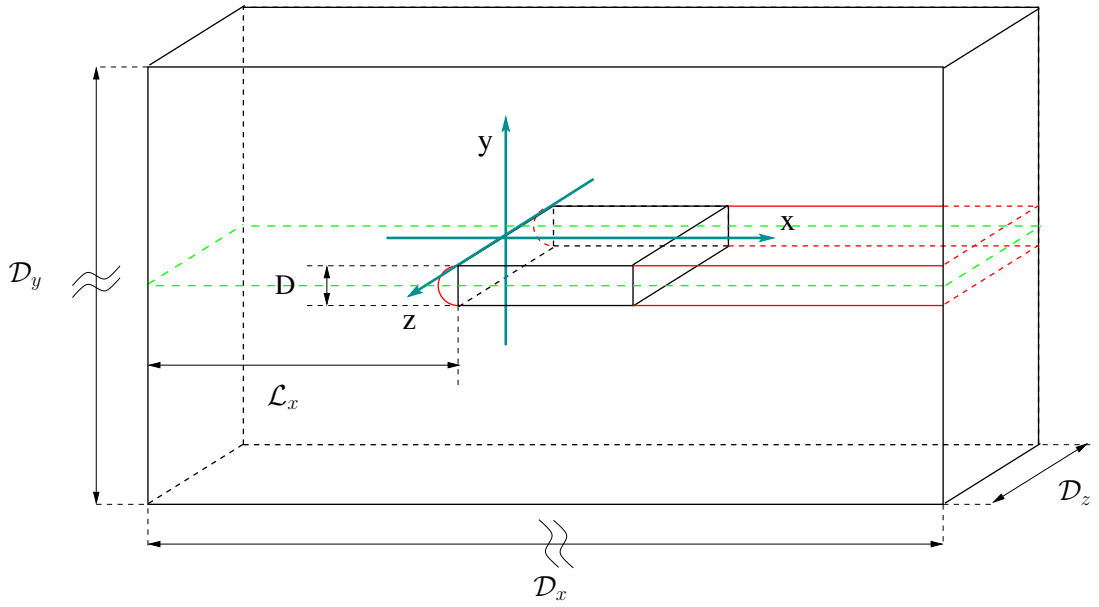

Figure 1: Configuration of the simulated flows. The geometry of the rectangular cylinder (*run1*) is shown with a black line while its extension without trailing edge (*run2*) is reported with a red line. The same red lines is used to show the flat plate geometry with circular leading edge (*run3*) also reported with a red line. The symmetry plane used for the simulation of half the domain of the flat plate with circular leading edge (*run4*) is highlighted with a green dashed line.

a system of ordinary differential equations can be written in the form

$$\mathbf{M}\frac{d\mathbf{U}}{dt} + \mathbf{R} = \mathbf{0} \tag{1}$$

being $\mathbf{U}$ the vector of degrees of freedom, $\mathbf{R}$ the residuals vector and $\mathbf{M}$ a modified mass matrix equal to the identity matrix apart from the entries corresponding to the pressure DoFs, which are zero. The system of ODE is advanced in time using a Linearly-implicit Rosenbrock-type Runge–Kutta scheme named ROSI2PW [12]. The scheme can be written in general as

$$\mathbf{U}^{(n+1)} = \mathbf{U}^n + \sum_{j=1}^{s} m_j \Delta\mathbf{U}_j, \tag{2}$$

$$\left(\frac{\mathbf{M}}{\gamma\Delta t} + \frac{\partial\mathbf{R}(\mathbf{U}^n)}{\partial\mathbf{U}}\right)\Delta\mathbf{U}_i = -\mathbf{R}\left(\mathbf{U}^n + \sum_{j=1}^{i-1} a_{ij}\Delta\mathbf{U}_j\right) - \frac{\mathbf{M}}{\Delta t}\sum_{j=1}^{i-1} c_{ij}\Delta\mathbf{U}_j, \tag{3}$$

with $i = 1, ..., s$, where s is the number of stages and m_j, a_{ij}, c_{ij} are the set of coefficients. Such strategy requires to solve a number of linear systems equal to the number of the stages. To this end, a p-multigrid (pMG) algorithm is employed as a preconditioner for a matrix-free (MF), flexible GMRES solver. Such strategy uses, as lower level smoothers, preconditioned iterative linear solvers acting on matrices, namely $\mathbf{A}_i$, built by using the

	BJ-MB	AS(1)-MB	BJ-MF	pMG-MF 3LVL	pMG-MF 4LVL
GMRES	115	72	115	5 (5)	4.2 (4.7)
CPU Ratio	1	1.11	0.95	0.47 (0.34)	0.39 (0.36)
Memory Ratio	1	1.60	0.60	0.15 (0.15)	0.27 (0.27)

Table 1: Computational efficiency of different solution strategies, *run*3 test case, using 540 Intel Xeon CPUs.

entries of $\mathbf{A} = (\gamma\Delta t)^{-1}\mathbf{M} + \partial\mathbf{R}/\partial\mathbf{U}$ corresponding to a lower order polynomial, i. Similarly, all the multigrid restriction and prolongation operations can be easily performed by selecting directly the appropriate DoFs. Note that the scaling law for the memory required by the allocation of $\mathbf{A}$ is k^6 [11]. Therefore the size of $\mathbf{A}_i$ is reasonably small for $i \ll k$. For instance, when $k = 6$, $\mathbf{A}_1$ is 441 times smaller than $\mathbf{A}$. For this reason the use of few multigrid levels with low order smoothers does not significantly affect the memory request. In addition, if an element-wise block-Jacobi (EWBJ) preconditioner, which employs the factorization of the block-diagonal portion (local to the element) of the iteration matrix and discards the memory consuming off-diagonal blocks, is adopted for the smoother of the finest level it is possible to obtain an effective but still memory saving strategy. Note hat the matrix-free approximation replaces the $\mathbf{A}$ matrix not only in the outer GMRES solver, but also in the finest level smoother. As a consequence, the explicit evaluation of the off-diagonal blocks of the Jacobian matrix can be performed at a reduced cost since they are solely needed to build the preconditioner smoothers for the coarser-space operators.

To prove the effectiveness of the proposed approach, Table 1 reports numerical experiments performed at $k = 6$ on the *run*3 test case and shows the average number of GMRES iterations to reach and unpreconditioned relative tolerance of 10^{-5}, as well the CPU time and the memory footprint of the solution strategies, both relative to a standard approach. These results were obtained using 15 nodes, each equipped with two 18-cores Intel Xeon E5-2697 CPUs, of the MARCONI A1 HPC cluster available at CINECA. Five solution strategies are here considered and compared. The first one, which is the reference and it is labelled as block-Jacobi matrix-based (BJ-MB), uses the analytical $\mathbf{A}$ matrix and performs the ILU(0) on the squared, domain-wise portion of the iteration matrix for preconditioning purposes. Such strategy looses efficiency as the number of domains increase. A second choice, which compensates partially this effect, is the Additive Schwartz method (AS). The idea is to increase the coupling between the domain partitions by duplicating a specified number of layers of elements on the partition boundaries. The ILU(0) is therefore performed in a larger partition-wise portion of the iteration matrix if compared to the BJ. The last results deal with the matrix-free implementation and with the use of a pMG preconditioning strategy. Firstly, the table puts in evidence that the use of the Additive Schwartz method increases both the CPU time and the memory footprint of the code despite reducing the number of GMRES iterations. This behaviour is not surprising, since the additional relative amount of memory required for the storage of the overlapping layer of elements raises decreasing the number of elements per partition (in this case 71), as well as the relative amount of communications. On the other hand, us-

ing the BJ preconditioner and a matrix-free strategy, which for such space discretization provides similar CPU times to that of a matrix-based one, allows to save almost the 40% of the memory footprint, since the factorization of the iteration matrix can be efficiently performed in place. As regards the use of pMG-MF preconditioners, two strategies employing three and four levels (LVL) have been assessed. In both the cases, on the coarsest level $k = 1$, an Additive Schwartz preconditioner and 30 GMRES iterations are employed, while the other levels ($k = 2, 6$ and $k = 2, 4, 6$ for the three and four levels, respectively) are smoothed using 8 iterations of EWBJ-preconditioned GMRES smoothers. Note that the use of an Additive Schwartz on the coarsest level increase the coupling between the domain partitions at a low computational cost. The values reported in brackets have been obtained by lagging the $\mathbf{A}_i$ matrices and all the preconditioners of the multigrids levels for three consecutive time steps. Such operation, thanks to the matrix free approach [11], does not influence the accuracy of the computation. It can be seen the pMG-MF preconditioner allows (i) up to an 85% memory footprint reduction if compared to the reference strategy, thanks to the use of block-diagonal smoothers on the finest level; (ii) a strong reduction in the average number of GMRES iterations and (iii) up to a 66% reduction in the CPU time. It is worth pointing out that the use of a four-level strategy, which increases only slightly the memory allocation but reduces the CPU time and the number of iterations, performs comparably to the three-level one when the Jacobian lagging is employed, which demonstrate that the use of a very high number of multigrid levels does not seem particularly important from the efficiency point of view in a matrix-free context. In other words, since the Jacobian evaluation is CPU demanding especially for very high order of polynomial approximations, it can be convenient to freeze its evaluation for more than a time step. In this circumstance, it is not guaranteed that the use of an updated and more effective preconditioner operator in every time step results in a CPU advantage due to the higher assembly costs.

3 RESULTS

In this section, a preliminary assessment of the main features of recirculating flows under different configurations by means of single-point statistics is reported. The parameters of the simulations are reported in table 2. For all the flow cases, an unperturbed free-stream velocity U_∞ is applied at the inlet and a pressure condition is used at the outlet. On the other hand, in the top and bottom boundaries a far field boundary condition is used for the flow cases *run1* and *run2* while a symmetry conditions is applied for *run3* and

Table 2: Parameters of the simulations

Case	Re	$\mathcal{L}_x$	$\mathcal{D}_x \times \mathcal{D}_y \times \mathcal{D}_z$	$N_{elements}$	k	Δt
run1	3000	35	$112 \times 50 \times 5$	47670	6	0.05
run2	3000	20	$36 \times 50 \times 5$	29538	6	0.05
run3	3450	12	$28 \times 17 \times 2$	38320	6	0.05
run4	3450	12	$28 \times 17 \times 2$	18820	6	0.05

run4. Finally a periodic boundary condition is applied in the spanwise direction. After reaching a statistical steady state, the simulations have been run for a time of the order of 300 characteristic time scales D/U_∞ in order to obtain a number of sampling sufficient for statistical convergence. For the symmetry of the problem, statistics are computed by averaging in time and in the spanwise direction.

3.1 Friction and pressure coefficients

We start the analysis by considering the behaviour of the friction coefficient, c_f. As shown in figure 2(a), the behaviour of the friction coefficient highlights significant differences between the different flows. The general trend of the friction coefficient conforms with the presence of a large scale recirculating region $c_f < 0$ followed by an attached forward boundary layer $c_f > 0$. The main differences between the different flow configurations come from the length of the main recirculating region and from the presence or not of a second smaller recirculating flow within it.

Starting from the last consideration, we observe that for the flow cases with right angle corners, *run1* and *run2*, the near-wall reverse flow induced by the large scale recirculating bubble, detaches forming a secondary smaller recirculation that can be recognized by the presence of positive values of friction for streamwise locations within the main separation bubble. In both cases, the secondary bubble starts around $x = 1.04$, however its length ℓ_{sv} is found to be slightly larger for the case of a finite plate *run1*, see table 3. This secondary flow is not observed for the cases with circular leading-edge corner, *run3* and *run4*. As shown in Cimarelli *et al.* [7], the presence of the secondary vortex is a result of adverse pressure gradient phenomena which induce the separation of the reverse boundary layer produced by the main recirculating flow. Accordingly, as shown in figure 2(b), the pressure coefficient highlights a negative streamwise gradient, $dc_p/dx < 0$, only for the flow cases with right angle corners *run1* and *run2*. Hence, only for these two flow cases, the reverse flow induced by the main recirculating bubble experiences an adverse pressure gradient. As a consequence, the reverse boundary layer detaches, thus leading to a secondary smaller recirculating region.

As far as it concerns the length of the main recirculating region, we observe that all the flow cases behave in a different way. In particular, as also shown in table 3, the reattachment length goes from the smallest value, $x_R = 3.88$, for the flow case *run3* to the largest one, $x_R = 4.81$, for the case *run2*. The reattachment length strongly depends on the turbulence levels created in the leading-edge shear layer which in turn are affected by the geometry of the leading-edge corner and by the presence/absence of trailing edge vortex shedding mechanisms as unequivocally shown here in quantitative terms.

Table 3: Reattachment lengths

	run1	*run2*	*run3*	*run4*
x_R	4.02	4.81	3.88	4.32
ℓ_{sv}	0.85	0.94	-	-

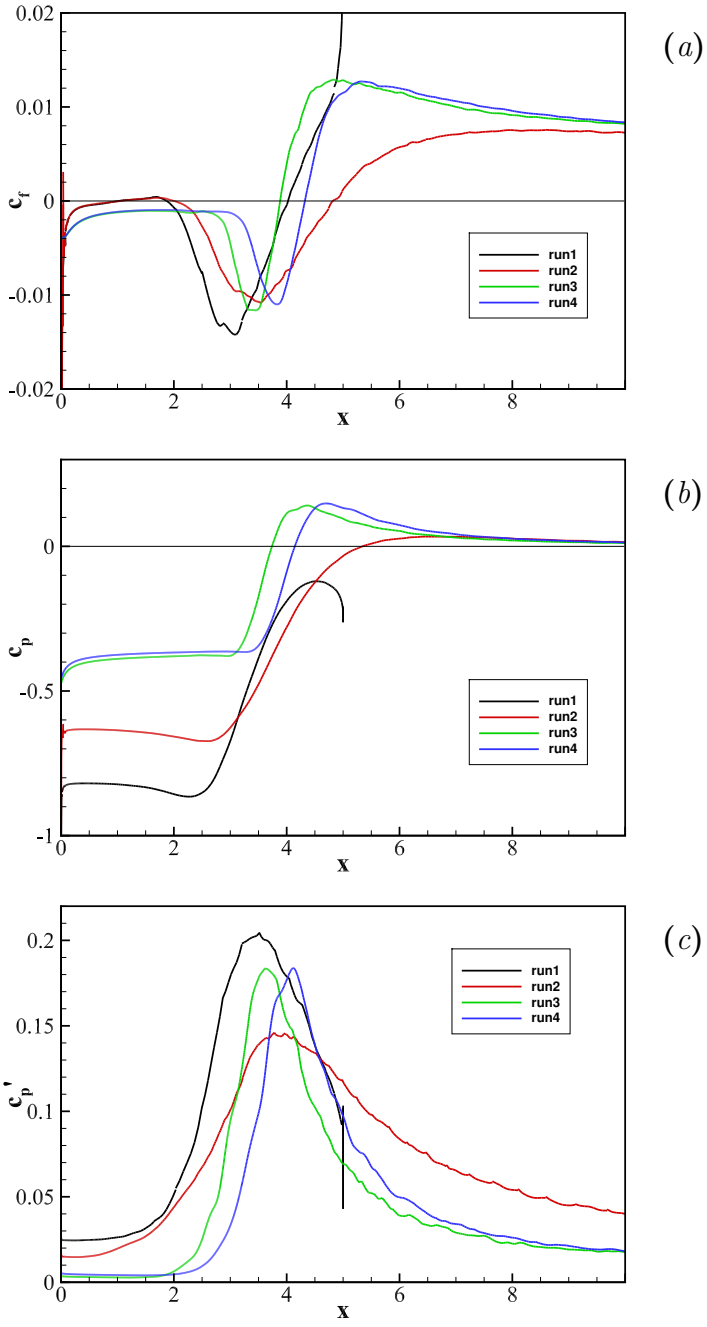

Figure 2: Streamnwise behaviour of the friction (a), pressure (b) coefficients in the different flow configurations simulated. The behaviour of the standard deviation of the pressure coefficient is also shown in (c).

It is worth pointing out that, as expected, in the upstream portion of the flat plates, the behaviour of the friction coefficient appears to be strongly affected by the geometry of the leading edge independently of the presence or not of a trailing edge flow separation. Indeed, similar behaviours are observed for the same geometry. On the other hand, while

moving downstream, the effect of the presence of the trailing-edge separation becomes relevant and a departure of the behaviour of the friction coefficient for the cases *run1* and *run2* is observed. Interestingly, when comparing cases *run3* and *run4*, one would expect that the effect of the presence/absence of a flow separation in the two sides of the plate is more relevant in the region close to the leading edge where the top and bottom sides of the plate communicate. However, as shown here in quantitative terms, the effect of the presence/absence of a flow separation in the two sides of the plate is negligible in the upstream part of the plate where the friction coefficient shows similar behaviour and a significant departure is observed only downstream. The same reasoning apply when comparing the downstream behaviour of the friction coefficient of flow cases *run2* and *run3*. Indeed, we would expect that the effect of the different leading-edge geometry is retained only in the upstream part of the plate. On the contrary, the differences are observed also downstream.

Let us consider now the behaviour of the pressure coefficient c_p and of its standard deviation c_p' shown in figure 2(b) and (c), respectively. As for the friction coefficient analysed so far, the leading-edge geometry is the most significant parameter influencing the upstream behaviour of the recirculating flow. Indeed, we observe that, both in terms of average and fluctuating intensity, the pressure field behaves similarly for the flow cases *run1*/*run2* and *run3*/*run4*. It consists in a flat behaviour of c_p associated with small value of c_p' for the circular leading-edge geometry. On the other hand, for right-angle corners, the pressure field c_p slightly decreases moving downstream the leading edge, $dc_p/dx < 0$, and the associated fluctuations, c_p' are more intense. Let us recall that, as previously shown when analysing the behaviour of the friction coefficient, the presence or not of a negative pressure gradient, $dc_p/dx < 0$, is at the basis of the formation or not of the secondary recirculating flow.

By moving downstream, the pressure recovery show significant differences which are particularly interesting for the flow cases without trailing edge separation, i.e. *run2*, *run3* and *run4*. Indeed, these flow cases differentiate for the geometry of the leading edge corner and for the presence or not of flow separation in the two sides of the plate. Such a differences are physically located upstream but their effects are significant also in the pressure recovery region downstream the reattachment. An homogenization of the pressure distribution between the different cases is recovered for $x > 7$ only for c_p since the intensity of the fluctuations c_p' remain different for longer distances.

3.2 Single-point statistics

The behaviour of the mean velocity field for the different flow configurations is shown in figure 3 with streamlines. We observe that the main recirculating region is strongly affected by the shape of the leading-edge corner. Indeed, sharp leading-edge corners, *run1* and *run2*, are found to produce thicker recirculating bubbles with respect to circular leading-edge corners. The effect of the trailing-edge separation consists in a reduction of the length of the recirculating zone, compare *run1* and *run2*. On the other hand, by comparing *run3* and *run4*, we observe that the effect of the presence or not of a separating flow in the two sides of the plate is less significant as far as it concerns the

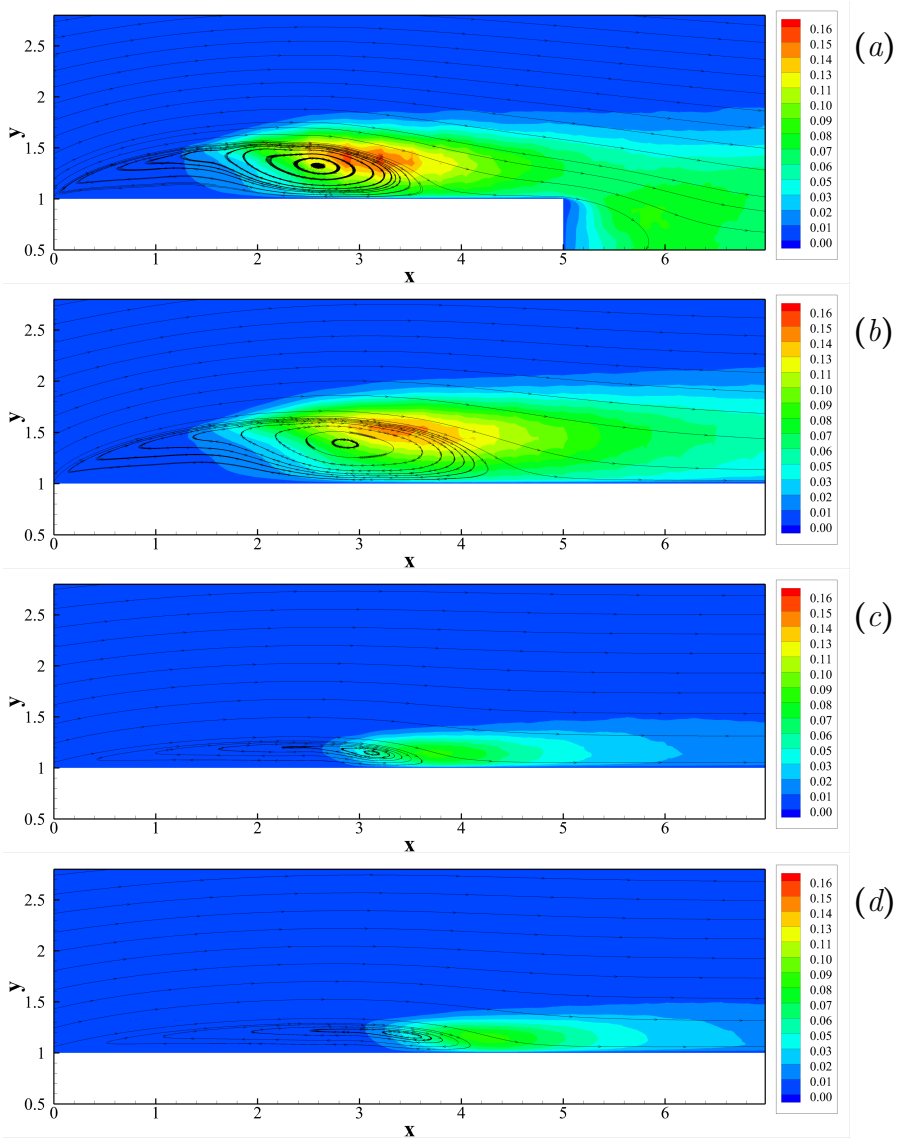

Figure 3: Mean velocity field streamlines and isocontour of turbulent kinetic energy. (a) *run1*. (b) *run2*. (c) *run3*. (d) *run4*.

height of the recirculating flow while a significant streamwise elongation is observed, see also the reattachment lengths reported in table 3.

Interesting insights can be argued by analysing the behaviour of the turbulent kinetic energy for the different flow configurations shown with isocontours in figure 3. It is evident how the presence of a sharp leading-edge corners, beside producing a thicker flow recirculation, leads to a faster transition to turbulence. In other words, the initially laminar leading-edge shear layer is found to develop instabilities and turbulence fluctuations, for streamwise locations which, for the case of sharp leading-edge corners, are significantly upstream with respect to smooth corners, compare the turbulent intensity levels of cases *run1* and *run2* to the cases *run3* and *run4*. This upstream shift of the main instabilities

giving rise to turbulent transition is associated also to more intense turbulent fluctuations . Indeed, for all the flow cases, the most intense fluctuations are reached in the shedding region of the main recirculating bubble but, as highlighted by the higher levels of isocontours, these maxima are stronger for flow with sharp leading-edge corners with respect to those with smooth corners. Beside the smaller extension of the induced recirculation, the effect of the flow separation at the trailing-edge is also to increase the intensity of the turbulent fluctuations, compare *run1* to *run2*.

In closing this section, let us focus the analysis on the effect of the presence or not of a flow separation in the two sides of the plate, cases *run3* and *run4*. Indeed, as already stated, the artificial removal of the possible interactions between the two sides of the plate leads to significantly longer recirculating regions. As it is well known from well-established literature results, see e.g. [18], longer recirculating regions are commonly associated with lower turbulence levels. However, as shown here in quantitative terms, the longer recirculating region of the flow case *run4* is associated with roughly the same levels of turbulent intensities of the flow case *run3*. Arguably, we conjecture that such a difference in the reattachment length is related with the presence or not of a large scale unsteadiness which takes the form of a flapping of the main recirculating bubble. The resulting enlargement and shrinkage of the main recirculation, once averaged, leads to a shorter mean reattachment length. The investigation of such a phenomenon is left to future works. However, let us point out that, if confirmed, the well-known very large scale unsteadiness could be explained as a phenomenon of connection between top and bottom flow instabilities which give rise to a self-sustained feedback mechanisms in the form of a flapping of the main recirculating bubble locked in phase opposition in the two sides of the plate.

4 CONCLUSIONS

In the present work, we exploit the ability of numerical simulations to manipulate the flow conditions in order to understand how geometrically relevant parameters influence the behaviour of separating and reattaching flows. To this aim we make use and prove the reliability of high-order Discontinuous Galerkin methods for the solution of transitional separating and reattaching phenomena.

The statistical analysis of the results reveals the role played by the leading-edge corner geometry. It is found that sharp leading-edge corners give rise to a thicker recirculating bubble and to the appearance of a secondary recirculating flow within it. This secondary motion is associated with the presence of a negative streamwise pressure gradient peculiar of sharp leading-edge corners. The picture is the following. The reverse flow induced by the main recirculating bubble experience an adverse pressure gradient and detaches thus giving rise to the secondary recirculation. The effects of the geometry of the leading-edge corner are analysed also in terms of turbulent fluctuations which are found to be more intense in the case of sharp corners. In particular, sharp corners are associated with an amplification of the instabilities of the leading-edge shear layer thus giving rise to a faster transition to turbulence.

The effect of the trailing-edge separation has been also analysed. It is found that

a flow separation at the trailing-edge induces a smaller flow recirculation probably due to the fact that the flow exploit more intense turbulent fluctuations. We argue that this behaviour could be the result of a coupling phenomenon between shedding of vortices from the recirculating bubble and from the trailing-edge which gives rise to a self-sustaining mechanism. To support this, we refer to a future work where also frequency spectra are taken into consideration.

Finally a preliminary study of the origin of the very-large scale unsteadiness of separating and reattaching flow is also reported. By analysing data from a simulation of the flow around half-flat plate with circular leading-edge corner, we are able to avoid the presence of a possible very large scale phenomenon of coupling of the flow separations occurring in the two sides of the plate. We observe that the inhibition of such a process leads to longer recirculating regions but retaining at the same time the same levels of turbulent intensity. Since, it is well-known that longer recirculating regions are associated with lower turbulence levels, we conjecture that the origin of such a difference comes from the presence of very long period of enlargement and shrinking of the main flow recirculation which leads to a shorter reattachment length on average. If confirmed, this phenomenon could take origin solely from a very large scale unsteadiness coupling the flow separation in the two sides of the plate. However, also in this case, we refer to a future work where frequency spectra are taken into consideration in order to provide more supporting evidence of the phenomenon.

REFERENCES

[1] Kiya, M. and Sasaki, K. Structure of large-scale vortices and unsteady reverse flow in the reattaching zone of a turbulent separation bubble. *J. Fluid Mech.* (1985) **154**, pp. 463–491.

[2] Stokes, A. N. and Welsh, M. C. Flow-resonant sound interaction in a duct containing a plate, II: square leading edge. *J. Sound Vib.* (1986) **104**, pp. 55–73.

[3] Nakamura, Y. and Ohya, Y. and Tsuruta, H. Experiments on vortex shedding from flat plates with square leading and trailing edges. *J. Fluid Mech.* (1991) **222**, pp. 437–447.

[4] Ohya, Y. and Nakamura, Y. and Ozono, S. and Tsuruta, H. and Nakayama, R. A numerical study of vortex shedding from flat plates with square leading and trailing edges. *J. Fluid Mech.* (1992) **236**, pp. 445–460.

[5] Hourigan, K. and Thompson, M. C. and Tan, B. T. Self-sustained oscillations in flows around long blunt plates. *J. Fluids Struct.* (2001) **15**, pp. 387–398.

[6] Mills, R. and Sheridan, J. and Hourigan, K. Particle image velocimetry and visualization of natural and forced flow around rectangular cylinders. *J. Fluid Mech.* (2003) **478**, pp. 299–323.

[7] Cimarelli, A. and Leonforte, A. and Angeli, D. Direct numerical simulation of the flow around a rectangular cylinder at a moderately high Reynolds number. *J. Wind Eng. Ind. Aerodyn.* (2018) **174**, pp. 39–49.

[8] Kiya, M. and Sasaki, K. Structure of a turbulent separation bubble. *J. Fluid Mech.* (1983) **137**, pp. 83–113.

[9] Cherry, N. J. and Hillier, R. and Latour, M. E. M. Unsteady measurements in a separated and reattaching flow. *J. Fluid Mech.* (1984) **144**, pp. 13–46.

[10] Sasaki, K. and Kiya, M. Three-dimensional vortex structure in a leading-edge separation bubble at moderate Reynolds numbers. *J. Fluids Eng.* (1991) **113**, pp. 405–410.

[11] Franciolini, M. and Crivellini, A. and Nigro, A. On the efficiency of a matrix-free linearly implicit time integration strategy for high order discontinuous Galerkin solution of incompressible turbulent flows. *Comput. Fluids* (2017) **159**, pp. 276–294.

[12] Rang, J. and Angermann, L. New Rosenbrock methods of order 3 for PDAEs of index 2. *Proceedings of Equadiff-11 2005* (2007), pp. 385–394.

[13] Crivellini, A. and Franciolini, M. and Nigro, A. An implicit Discontinuous Galerkin method with reduced memory footprint for the simulation of turbulent flows. To appear in *Direct and Large-Eddy Simulation XI*.

[14] Bassi, F. and Crivellini, A. and Di Pietro, D. A. and Rebay, S. An artificial compressibility flux for the discontinuous Galerkin solution of the incompressible Navier-Stokes equations. *J. Comput. Phys.* (2006) **218**, pp. 794–815.

[15] Bassi, F. and Crivellini, A. and Di Pietro, D. A. and Rebay, S. An implicit high-order discontinuous Galerkin method for steady and unsteady incompressible flows. *Comput. Fluids* (2007) **36**, pp. 1529–1546.

[16] Bassi, F. and Rebay S. and Mariotti G. and Pedinotti, S. and Savini, M. A high-order accurate discontinuous finite element method for inviscid and viscous turbomachinery flows. *Proceedings of the 2nd European Conference on Turbomachinery Fluid Dynamics and Thermodynamics* (1997),pp. 99–108.

[17] Crivellini, A. and D'Alessandro, V. and Bassi, F. Assessment of a high-order discontinuous Galerkin method for incompressible three–dimensional Navier–Stokes equations: Benchmark results for the flow past a sphere up to Re=500. *Comput. Fluids* (2013) **86**, pp. 442 - 458.

[18] Saathoff, P. J. and Melbourne, W. H. Effects of free-stream turbulence on surface pressure fluctuations in a separation bubble. *J. Fluid Mech.* (1997) **337**, pp. 1–24.